land

MDPI

Article

Deep Learning Based Spatial Distribution Estimation of Soil Pb Using Multi-Phase Multispectral Remote Sensing Images in a Mining Area

Min Tan [1], Xiaotong Zhang [2,3], Weiqiang Luo [2,3] and Ming Hao [2,3,*]

[1] School of Public Policy and Management (School of Emergency Management), China University of Mining and Technology, Xuzhou 221116, China; db16160031b0@cumt.edu.cn
[2] School of Environment and Spatial Informatics, China University of Mining and Technology, Xuzhou 221116, China; ts21160208p31@cumt.edu.cn (X.Z.); ts22160042a31@cumt.edu.cn (W.L.)
[3] Jiangsu Key Laboratory of Resources and Environmental Information Engineering, China University of Mining and Technology, Xuzhou 221116, China
* Correspondence: haoming@cumt.edu.cn

Abstract: Extensive investigation and monitoring of lead (Pb) content of soil is significant for ensuring hazard-free agricultural production, protecting human health, and ecosystem security, especially in a mining area. One temporal period of a hyperspectral image is usually used to estimate the spatial distribution of Pb and other heavy metals, but hyperspectral images are usually difficult to obtain. Multispectral remote-sensing images are more accessible than hyperspectral images. In this study, a deep learning-based model using 3D convolution is proposed to estimate the Pb content from the constructed multi-phase, multispectral remote-sensing images. Multi-phase multispectral remote-sensing images were stacked to generate a data set with more spectral bands to reduce the atmospheric absorptive aerosol effect. At the same time, a neural network based on 3D convolution (3D-ConvNet) was proposed to estimate Pb content based on the constructed data set. Compared with partial least-squares regression (PLSR), random forest regression (RFR), support vector machine regression (SVMR), and gradient-boosting regression (GBR), experimental results showed the proposed 3D-ConvNet has obvious superiority and generates more accurate estimation results, with the prediction dataset coefficient of determination (R^2) and the mean normalized bias (MNB) values being 0.90 and 2.63%, respectively. Therefore, it is possible to effectively estimate heavy metal content from multi-phase, multispectral remote-sensing images, and this study provides a new approach to heavy metal pollution monitoring.

Keywords: multi-phase; multispectral images; heavy metal content estimation; deep learning-based regression; 3D convolution

check for updates

Citation: Tan, M.; Zhang, X.; Luo, W.; Hao, M. Deep Learning Based Spatial Distribution Estimation of Soil Pb Using Multi-Phase Multispectral Remote Sensing Images in a Mining Area. *Land* **2023**, *12*, 1789. https://doi.org/10.3390/land12091789

Academic Editor: Evangelia Golia

Received: 29 July 2023
Revised: 4 September 2023
Accepted: 11 September 2023
Published: 15 September 2023

Copyright: © 2023 by the authors. Licensee MDPI, Basel, Switzerland. This article is an open access article distributed under the terms and conditions of the Creative Commons Attribution (CC BY) license (https://creativecommons.org/licenses/by/4.0/).

1. Introduction

Soil heavy metal pollution has become a global problem, especially in mining cities, where heavy metal pollution is particularly serious. During coal mining, the long-term stacking of coal gangue and the wastewater discharge pose a certain threat to the surrounding environment of the mining area, resulting in excessive heavy metal content in soil, water, and vegetation [1]. The sewage irrigation and excessive use of pesticides and fertilizers in the surrounding farmland further aggravate the heavy metal pollution [2].

Lead (Pb) is a common heavy metal pollutant in the soil of mining areas. It has poor mobility once it infiltrates the soil and is characterized by a long impact cycle and non-biodegradability. It tends to accumulate in the soil, sediments, water bodies, atmosphere, staple crops, and vital organs of the human body over a long period of time [3]. When the concentration of heavy metals exceeds the environmental carrying capacity, they can disrupt the environment, pose a threat to the health of humans and other organisms, impact

microbial diversity and community structure, and disrupt ecological balance [4]. Therefore, extensive investigation and monitoring of Pb content in soil is of great significance for ensuring agricultural production, protecting human health, and ecosystem security [5,6].

Although the traditional laboratory chemical analysis method based on field sampling has high precision, it is time-consuming and costly, and it is difficult to realize the spatiotemporal dynamic monitoring of the heavy metal distribution in a large area. Hyperspectral remote sensing can obtain the reflection spectral curve of ground objects with continuous-band and hyperspectral resolution, which enables continuous, temporal, and spatial mapping of soil heavy metal distribution in a large-scale area [7].

Machine learning methods have the advantage of solving complex nonlinear problems and have been applied to the content estimation of heavy metals from hyperspectral remote sensing. Partial least-squares regression (PLSR) was used to estimate Pb content in soil based on remote-sensing spectroscopy, which has been widely used in soil element estimation [8–10]. Support vector machine regression (SVMR) is a regression method based on a support vector machine (SVM), which can handle nonlinear regression problems and is robust to outliers. Therefore, it has been a popular method for estimating heavy metals using hyperspectral data [11,12]. Random forest is an ensemble learning algorithm, and the final result is voted on or averaged by combining multiple weak classifiers. Therefore, the results have high accuracy and generalization performance, and random forest regression (RFR) showed effective performance for estimating Pb and other heavy metal contents [13–15]. Gradient-boosting regression (GBR) is also a very important algorithm in ensemble learning that can reduce the cumulative model loss of weak learners in the direction of a negative gradient and improve the accuracy of regression results. It has been used to estimate As content in soils from hyperspectral reflection and can obtain a better inversion effect than PLSR, SVMR, and RF with fewer characteristic bands [16]. In addition, decision trees [17], extreme learning machines [18], and artificial neural networks [19] were also implemented to estimate heavy metal contents in the soil.

Deep learning has shown an advantage over traditional machine learning methods in the classification of high-resolution and hyperspectral remote-sensing images [20–22] due to its ability to extract deep spatial and spectral features. The methods of deep learning have also been used in environmental monitoring using multi-spectral remote-sensing images, and effective performances have been shown in many studies [23,24]. Wei et al. used competitive adaptive reweighted sampling to improve the deep neural network for estimating TA content in soils based on UAV hyperspectral imagery [25]. Ou et al. proposed a semi-supervised deep neural network regression method based on airborne hyperspectral images to estimate heavy metals [26]. Compared with DNN, the convolutional neural network (CNN) model uses convolutional layers, replacing independent neurons in DNN, to simultaneously obtain spatial and spectral features from multispectral and hyperspectral images and generate accurate classification results [27,28]. Pyo et al. estimated the concentrations of phycocyanin and chlorophyll-a based on the hyperspectral image using a CNN model [29]. Niu et al. implemented pixel- and patch-based CNN regression models to predict inactive water quality parameters using airborne hyperspectral imagery [30]. A CNN-based regression model was proposed to estimate the macronutrient distribution in a cornfield using the normalized difference vegetation index (NDVI) of images obtained by a UAV [31]. The above studies have shown that CNN models have the advantage of extracting features from high-dimensional data and obtaining a reasonable spatial distribution result. For most studies based on CNN, two-dimensional convolution is often used to extract features, but its ability to mine correlation information between spectral bands and process redundant information between bands is insufficient.

Hyperspectral features of visible and near-infrared reflectance have been widely used as input data to estimate heavy metal content in the existing literature [32,33]. The hyperspectral information is usually obtained in the field, including with a handheld spectrometer [34,35], a hyperspectral imaging sensor on an unmanned aerial vehicle (UAV) [23,25], an airplane [14,30,36], and a satellite [13,37]. However, hyperspectral images are usually

difficult to obtain due to fewer hyperspectral satellites and expensive hyperspectral sensor equipment. In this study, a deep learning-based model using a three-dimensional convolution network (3D-ConvNet), is proposed to estimate the heavy metal from constructed multi-phase remote sensing data, which was generated by stacking multi-phase, multispectral remote sensing images. On the one hand, the constructed data set is easier to access; on the other hand, the influence of atmospheric radiation on the spectral characteristics can be reduced by adding multi-period images to enhance the characteristics of the spectrum. A neural network based on 3D convolution was proposed to simultaneously extract deep spatial–spectral–temporal features, which makes the regression model more effective. The contributions of this study were: (1) to investigate the use of constructed multi-phase, multispectral remote sensing images to estimate the heavy metal content; (2) to compare the accuracy of the 3D convolution based on a deep learning regression method with that of the traditional regression methods (PLSR, RFR, SVMR, and GBRT); and (3) to generate a spatial distribution map of Pb in the study area.

2. Materials

2.1. Study Area

This study focuses on Peixian County in Xuzhou City, Jiangsu Province, with geographic coordinates ranging from 34°28′ to 34°59′ N and 116°41′ to 117°09′ E. The total area of the study area is approximately 1806 square kilometers, and the location of Peixian County is shown in Figure 1. Peixian County is located in the high groundwater level area of eastern China, within Xuzhou City, Jiangsu Province. It is a typical coal and grain compound region with 8 coal mines and a large subsidence area. Peixian County has a temperate, semi-humid monsoon climate with four distinct seasons. The soil is primarily meadow soil, and wheat and maize are cultivated twice a year with a continuous yield exceeding 15 tons per hectare for the past ten years. With 7 coal mines, Peixian County is currently the only coal production base in Jiangsu Province. The specific locations of the Sanhejian (SHJ) coal mine, Longdong (LD) coal mine, Yaoqiao (YQ) coal mine, Zhangshuanglou (ZSL) coal mine, Xuzhuang (XZ) coal mine, Kongzhuang (KZ) coal mine, and Peicheng (PC) coal mine can be seen in Figure 1. The proven coal reserves amount to 2.37 billion tons [38].

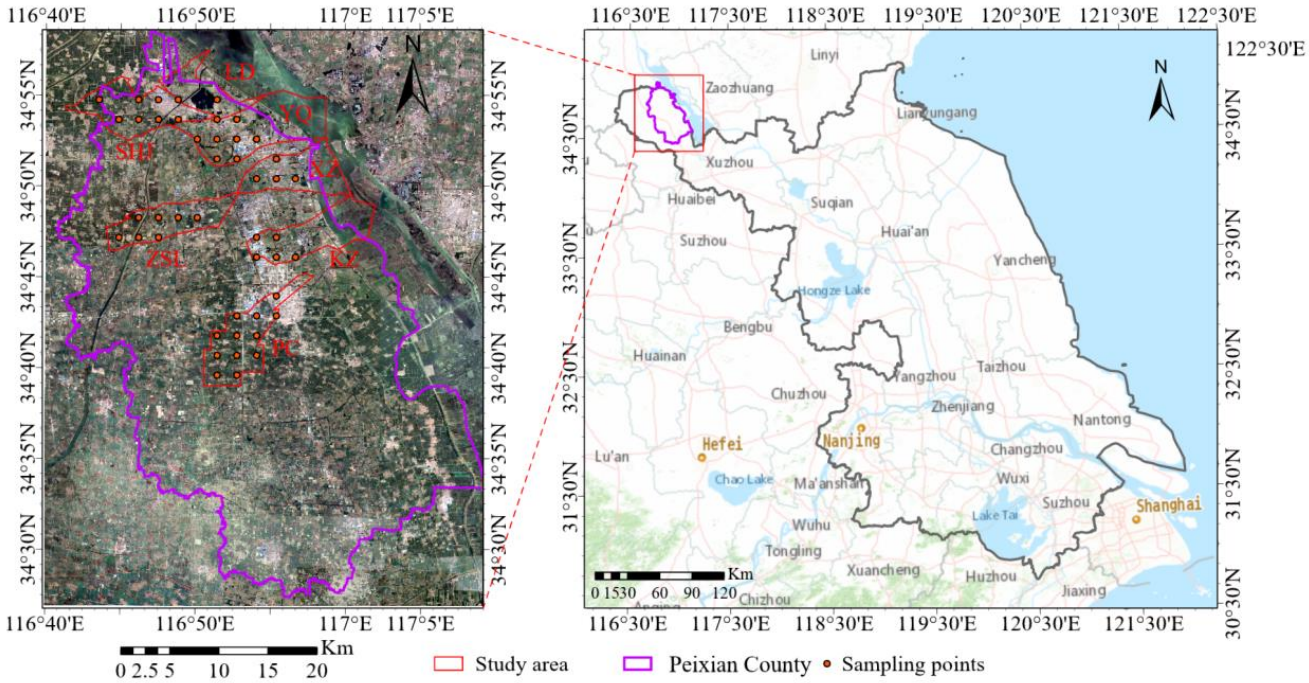


Figure 1. Geographic location of Peixian County and sampling positions.

2.2. Soil Heavy Metal Data

This study is based on 45 soil samples from the Second National Soil Survey of China and aims to investigate the spatial distribution characteristics of Pb in the soil of mining areas (Figure 1). During sample collection, the study area was divided into a grid of 2 km × 2 km, and three sub-samples of soil were collected within each grid and mixed uniformly. The surface soil samples (0–20 cm) were collected using a hand shovel, placed in sealed bags, stored in ice packs, and transported to the laboratory.

Before conducting the analysis, the soil samples were air-dried at room temperature, typically taking 7–10 days for complete drying. The soil was then broken into small clumps with a diameter smaller than 1 cm along the natural structure (fissures) of the soil, removing gravel and plant debris. The soil was then sieved using a 2 mm mesh screen and stored in polyethylene bags at a temperature of 4 °C. After pre-treatment, the soil and sediment were subjected to high-temperature digestion using HNO_3-HCl-HF (3:3:2) and analyzed for the content of Pb using inductively coupled plasma-atomic emission spectroscopy (ICP-AES). The statistics of Pb content in different mining areas are shown in Table 1.

Table 1. Statistics of Pb content of samples in different mining areas (μg/g): numbers (No.), maximum (max), minimum (min), and standard deviation (std).

Mining Area	No.	Max	Min	Std
SHJ	7	19.4	15.5	1.32
LD	3	22.6	17.5	2.11
YQ	7	21.6	16.4	1.74
ZSL	7	18.2	15.9	0.72
XZ	4	26.6	18.3	3.16
KZ	5	25.7	21.1	1.66
PC	12	28.5	18.4	2.62

2.3. Experimemtal Images

In this study, multi-spectral remote sensing images obtained by Landsat 7 ETM+ and Landsat 8 OLI in 2014 were used as the data source. The final images were selected from the above images with cloud cover less than 3% in the study area, as shown in Table 2, which consists of 5 Landsat 8 OLI images and 6 Landsat 7 ETM+ images. The 1–7 bands of Landsat 8 OLI images and the 1–5 and 7 bands of Landsat 7 ETM+ images (excluding the thermal infrared band) were used for the regression. The images were atmospherically corrected using the FLAASH model and then registered using a polynomial registration model. All the multispectral images were stacked in chronological order to generate a final remote sensing dataset with 71 bands for the heavy metal estimation.

Table 2. Remote sensing images used in this study.

No. of Images	Sensor	Date	Used Bands and Wavelength (μm)
1	Landsat7 ETM SLC-off	13 March 2014	1/0.45~0.515
2	Landsat7 ETM SLC-off	14 April 2014	2/0.525~0.605
3	Landsat7 ETM SLC-off	30 April 2014	3/0.63~0.690
4	Landsat7 ETM SLC-off	4 August 2014	4/0.75~0.90
5	Landsat7 ETM SLC-off	21 September 2014	5/1.55~1.75
6	Landsat7 ETM SLC-off	7 October 2014	7/2.09~2.35

Table 2. *Cont.*

No. of Images	Sensor	Date	Used Bands and Wavelength (μm)
7	Landsat 8 OLI TIRS	21 March 2014	1/0.433~0.453
8	Landsat 8 OLI TIRS	2 December 2014	2/0.450~0.515
9	Landsat 8 OLI TIRS	2 December 2014	3/0.525~0.600
10	Landsat 8 OLI TIRS	18 December 2014	4/0.630~0.680
11	Landsat 8 OLI TIRS	18 December 2014	5/0.845~0.885
			6/1.560~1.660
			7/2.100~2.300

3. Methods

3.1. Proposed 3D-ConvNet for Heavy Metal Estimation

As shown in Figure 2, the proposed 3D-ConvNet model for heavy metal estimation consists of three steps:

1. Constructing the multi-temporal remote sensing data set;
2. Building a deep neural network using a 3D convolutional algorithm;
3. Training the deep neural network based on samples and estimating the heavy metal content based on the constructed multi-temporal image.

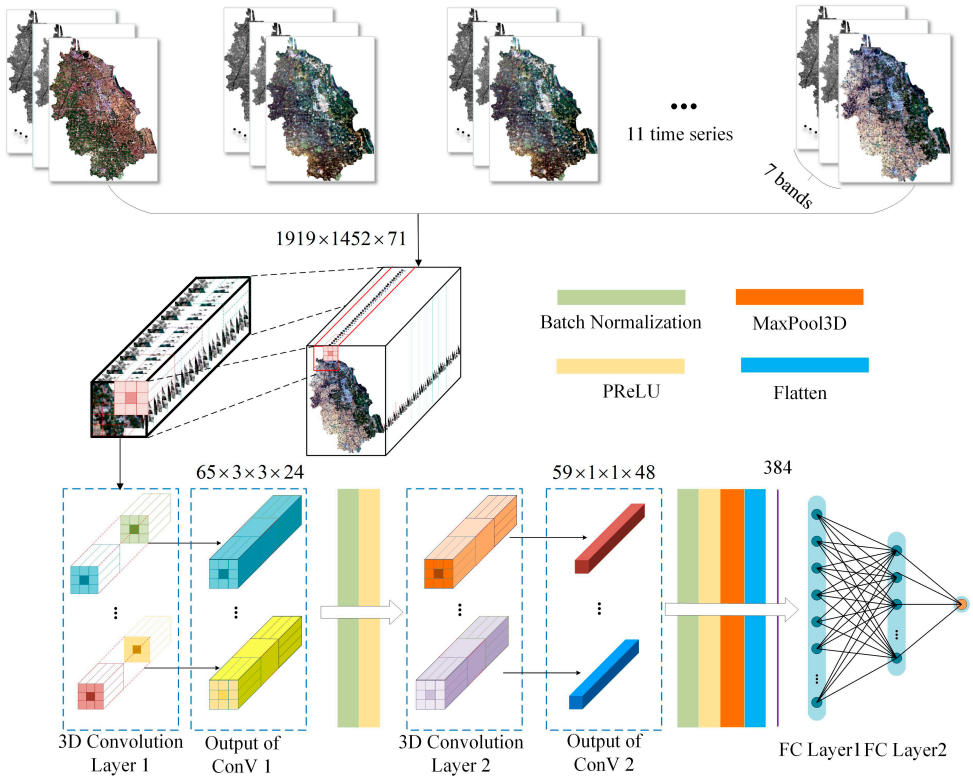


Figure 2. Flowchart of the proposed 3D-ConvNet model.

3.1.1. Constructing the Multi-Temporal Remote Sensing Data Set

The single-temporal multispectral image is easily affected by atmospheric conditions and land cover, and it has less spectral information. The multi-phase images can provide more information, and the estimation results are robust. Therefore, multi-phase Landsat images were used in this study.

The heavy metal concentration in the soil remains relatively stable over a short period of time [1,3]. Therefore, this study collected multi-temporal remote sensing images from the same year as the field sampling. These images were processed, including atmospheric

correction, registration, and cropping [39], and stacked to generate a remote sensing dataset with multiple spectral information bands. The gapfill plug-in in ENVI (5.3) software was used to repair the missing strip data in Landsat 7 ETM SLC-OFF images by the interpolation method. Only multi-spectral images without cloud cover over the study area were used in this study, and the unbalanced interval of time phases caused by cloud cover was not considered in this study.

By utilizing multi-temporal and multi-spectral remote sensing images, a high-dimensional remote sensing dataset was constructed for heavy metal estimation. By incorporating additional data sources, it partially overcame the limitation of low spectral resolution in multi-spectral images and enhanced the reliability of the estimation results.

3.1.2. Building a Deep Neural Network Using a 3D Convolutional Algorithm

A novel, deep neural network was constructed based on a multilayer 3D convolutional algorithm for spatial–spectral–temporal feature learning from the constructed multi-temporal dataset.

First, the neighboring cubes of pixels were obtained and used as input for the proposed network. For a pixel $P(i, j)$ located at (i, j) on the multi-temporal dataset, a patch of size $s \times s$ centered at (i, j) was generated with the spatial information. The patch had three dimensions: height, width, and depth, and the same channels as the multi-temporal dataset containing spatial–spectral–temporal features. It is worth noting that the size of the obtained patch affects the learning effectiveness of the neural network model. Existing studies have indicated that it is better for extracting nonlinear spatial features using relatively smaller regression patch sizes (8×8) [29]. Therefore, the size of the input patch was optimized and set to 5×5 in this study due to the spatial resolution of the used images.

Second, the generated patch was fed into the proposed neural network, and stacked 3D convolutional layers were designed after the input layer. CNN was originally designed for 2D image feature recognition, successfully creating a correlation between low-level signals and high-level semantics, and is widely applied in visual image classification and recognition. However, when dealing with 3D data, 2D convolutional neural networks have certain limitations in feature extraction. In this study, 3D convolution was implemented to process the multi-temporal hyperspectral data set, extracting spectral details from the multi-temporal hyperspectral image and incorporating temporal correlation information from the temporal dimension, which resulted in a data cube with multi-band and multi-temporal features. Three-dimensional convolution is more efficient and effective at extracting details than 2D convolution. Therefore, 3D convolution was used in 3D convolutional layers to learn the spatial–spectral–temporal features within a spatial neighborhood for the regression. The detailed process of 3D convolution is shown in Figure 3.

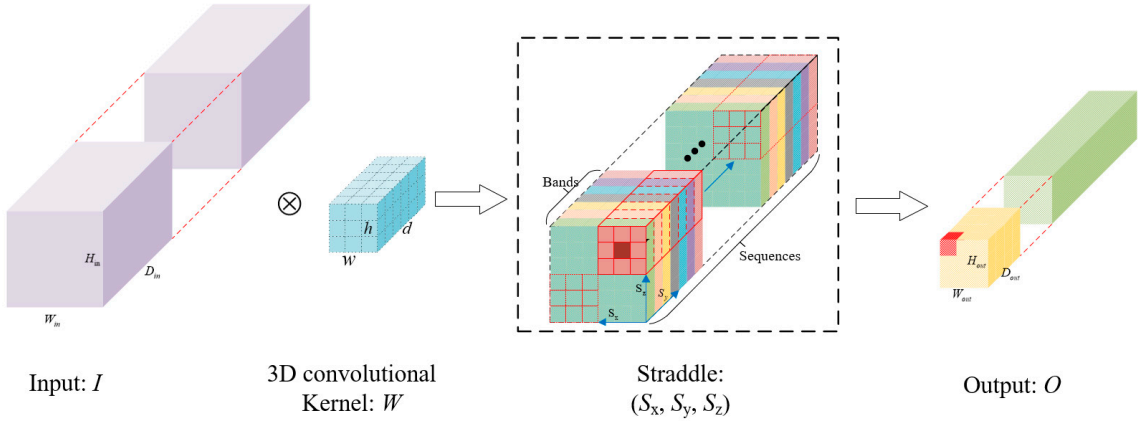


Figure 3. Illustration of 3D convolution.

As shown in Figure 3, the input data is denoted as $I \epsilon h^3$, with a size of $W_{in} \times H_{in} \times D_{in}$. A convolutional kernel $W \epsilon h^3 (w \leq W_{in}, h \leq H_{in}, d \leq D_{in})$ is used for the convolution operation. The convolution output is calculated using Equation (1).

$$O^{x,y,z} = b + \sum_{p=0}^{w-1} \sum_{q=0}^{h-1} \sum_{r=0}^{d-1} W^{p,q,r} I^{x*s+p,y*s+q,z*s+r}$$
$$x = 1, 2, \ldots, W_{out} \quad y = 1, 2, \ldots, H_{out} \quad z = 1, 2, \ldots, D_{out} \tag{1}$$

In the equation, $O^{x,y,z}$ represents the result at position (x, y, z) in the output O. Here, s represents the stride, b represents the bias, W_{out}, H_{out}, and D_{out} denote the size of the output O and are calculated using the following equations:

$$W_{out} = \frac{W_{in} + 2p - w}{s_x} + 1 \tag{2}$$

$$H_{out} = \frac{H_{in} + 2p - h}{s_y} + 1 \tag{3}$$

$$D_{out} = \frac{D_{in} + 2p - d}{s_z} + 1 \tag{4}$$

When 3D convolution was performed on the multi-temporal hyperspectral dataset, the convolution was carried out simultaneously in the spatial, spectral, and temporal domains, extracting spatial, temporal, and spectral features. To obtain different types of feature maps, multiple convolutional kernels were used in parallel during the convolution operation. Therefore, multiple feature maps $O_{i,j}^{x,y,z}$ were obtained with spatial, spectral, and temporal characteristics.

After the 3D convolutional layers, three-dimensional batch normalization was applied to normalize the features generated by each layer of 3D convolution, ensuring that the feature weights were within the same range. This allowed for the use of larger learning rates to accelerate the training process [40,41]. The PReLU activation function was used in the convolutional layers, which is an element-wise operation that improves model fitting by introducing a non-flat space structure without incurring additional computational cost or risking overfitting [42].

As shown in Figure 2, 3D convolutional layers, 3D batch normalization, and the PReLU activation function were implemented again to extract more meaningful features. Finally, local features explored by various 3D convolution filters were gathered using 3D max pooling. The extracted deep features were flattened and fed into three fully connected layers, in which the final output value was the heavy metal concentration. As a result, the parameter concentration was estimated through the proposed regression model by fully using spatial–spectral–temporal features.

3.2. Comparative Regression Methods

For heavy metal estimation based on spectral information, PLSR, SVMR, RFR, and GBR are widely used estimation algorithms. Therefore, the above four methods were compared with the proposed method to verify the effectiveness of the proposed method. The last three nonlinear regression methods and their parameters were introduced as follows:

3.2.1. Support Vector Machine Regression (SVMR)

SVMR is a regression model based on support vector machines (SVMs) [43] and has been widely used in the content estimation of heavy metals and demonstrated its advantages [30]. An ideal approximating hyperplane within a feature space of high dimensions was achieved to estimate the linear relationship between input vectors of n dimensions and a single output variable [44]. The radial basis function (RBF) is used as the kernel function to map the data to a high-dimensional feature space. The optimization of the penalty parameter C and the kernel function parameter g was performed during the training of

SVMR. Some studies have indicated that cross-validation combined with grid search is an effective method to optimize the parameters C and g [45]. In this study, the constructed multi-phase image was used as the input data, and SVMR was usually optimized by grid search [25,46,47]. The RBF was used as the kernel type of SVMR, and the parameters C and g were set from 0.01 to 3000 and 0.001 to 100, respectively.

3.2.2. Random Forest Regression (RFR)

RFR consists of multiple-decision-tree models to achieve classification, where an independent and identically random vector needs to be set. Under a given set of independent variables X, many prediction results are obtained by decision tree regression models [48]. In the RF regression, bootstrap sampling is employed to select k samples from the original measured spectral training set. The number of samples remains the same as that of the original training set. K decision-tree models are constructed using these samples, yielding K regression outcomes. The final prediction result is obtained by averaging these k results [16]. In this study, the constructed multi-phase image was used as the input data. RFR was optimized via grid search [25,46,47] The number of trees in RF was set from 50 to 200, and the max depth was set from 1 to 200.

3.2.3. Gradient-Boosting Regression (GBR)

Gradient-boosting produces classification and regression results by optimizing the error function. It generates a predictive model based on weak predictive models, such as decision trees [49]. In this algorithm, each iteration is accomplished by a base model, followed by the next iteration, which reduces the errors of the previous model and creates a new base model in the direction of the gradient of the residual reduction. Therefore, by continuously adjusting and optimizing the weights of the weak learners, it transforms them into strong learners, minimizing and optimizing the loss function [16]. The constructed multi-phase image was used as the input data.

3.3. Model Evaluation

The parameters of the prediction dataset coefficient of determination (R^2), root mean square error (*RMSE*), mean absolute error (*MAE*), and the mean normalized bias (*MNB*) were used to evaluate the performance of regression models used in this study. These metrics were employed to assess the model's predictive performance, and the smaller these indices, the better the predictive ability of the model. The indices were calculated as follows:

$$R^2 = 1 - \frac{\sum_{i=1}^{n}(y_i - \hat{y}_i)^2}{\sum_{i=1}^{n}(y_i - \overline{y}_i)^2} \tag{5}$$

$$RMSE = \sqrt{\frac{\sum_{i=1}^{n}(y_i - \hat{y}_i)^2}{n}} \tag{6}$$

$$MAE = \frac{1}{n}\sum_{i=1}^{n}|y_i - \hat{y}_i| \tag{7}$$

$$MNB = \frac{1}{n}\sum_{i=1}^{n}\frac{|y_i - \hat{y}_i|}{y_i} \times 100\% \tag{8}$$

where y_i is the measured value, $\hat{y}_i$ is the predicted value, and n is the sampling number.

4. Experimental Results and Analysis

4.1. Experimemtal Parameter Settings

The parameter settings of the designed 3D-ConvNet regression model are listed in Table 3. We empirically adjusted the learning rate, number of epochs, and filter size parameters using cross-validation. The network was trained on a Geforce GTX 2080TI GPU for 200 epochs with a learning rate of 0.01. To learn the spatial–spectral–temporal

characteristics of a pixel, the network was trained using a 5 × 5 neighborhood of pixels. To ensure the inclusion of border pixels, mirror padding was applied. Furthermore, the dataset was randomly split into training and test sets, maintaining a ratio of 2:1. The parameters of PLSR were usually optimized via grid search [25,46,47]. Therefore, the competent n of PLSR was set from 2 to 270.

Table 3. Parameters of the designed 3D-ConvNet regression model.

Layer Name	Input Size	Kernel Size	Strides	Output Size
3D Convolutional layer 1	71 × 5 × 5 × 1	7 × 3 × 3 × 24	1× 1 × 1 × 1	65 × 3 × 3 × 24
Batch normalization 1	65 × 3 × 3 × 24	—	—	65 × 3 × 3 × 24
3D Convolutional layer 2	65 × 3 × 3 × 24	7 × 3 × 3 × 48	1× 1 × 1 × 1	59 × 1× 1 × 48
Batch normalization 2	59 × 1× 1 × 48	—	—	59 × 1× 1 × 48
Pool 1	59 × 1× 1 × 48	7 × 1× 1	7 × 1× 1	8 × 1 × 1 × 48
Fully connected layer 1	8 × 1 × 1 × 48	—	—	1 × 64
Fully connected layer 2	1 × 64	—	—	1 × 10
Fully connected layer 3	1 × 10	—	—	1 × 1

4.2. Comparative Analysis of the Heavy Metal Estimation Models

The heavy metal Pb was estimated using PLSR, SVMR, RFR, GBR, and the proposed 3D-ConvNet for the regression from the single-phase image and the constructed multiple-phase images, respectively. The multi-spectral Landsat 7 image obtained on 7th October was used as the single-phase image due to the fact that its obtained date was the closest to the sampling date. Each sample was predicted by the above models after passing the cross-validation, and the regression results for Pb are listed in Table 4, respectively.

Table 4. Evaluation results of different models for the single-phase image (obtained on 7 October 2014) and multi-phase images.

Method	Single-Phase				Multi-Phase			
	R^2	*RMSE*	*MAE*	*MNB*	R^2	*RMSE*	*MAE*	*MNB*
PLSR	0.32	3.02	1.43	7.25%	0.41	2.71	1.05	5.73%
SVMR	0.54	1.92	1.62	7.83%	0.71	1.63	1.22	6.45%
RFR	0.60	1.73	1.54	7.36%	0.72	1.63	1.23	5.76%
GBR	0.69	1.54	1.31	6.63%	0.81	1.19	0.86	4.79%
3D-ConvNet	0.82	1.22	0.94	4.57%	0.90	0.89	0.49	2.63%

As for the Pb content estimation with the single-phase image, PLSR produced the estimation result with the lowest accuracy, and 3D-ConvNet generated the most accurate estimation result, with the R^2 and *MNB* being 0.82 and 4.57%, respectively. The estimation results from the multi-phase images were all improved compared to the corresponding model based on the single-phase image. The 3D-ConvNet obtained the highest accuracy of the estimation result, where the values of R^2 and *MNB* achieved 0.90 and 2.63%, respectively. Therefore, it was indicated that the constructed multi-phase data can provide more effective information and improve the estimation accuracy.

As for the Pb content estimation based on the multi-phase data, the PLSR model generated a low accuracy, which shows that the relationship between the constructed multi-spectral remote sensing dataset and Pb is not simply linear. As commonly used soil spectral prediction models, RFR and SVMR performed similarly and obtained similar results, with the R^2 being 0.71. But the value of *MNB* in RFR was lower than that of SVMR. The results are consistent with previous studies that used handheld spectrometers [12,16], but lower than the R^2 of handheld spectrometers used in previous studies, which was approximately 0.8 [13]. GBR showed good regression performance, with the R^2 and *MNB* being 0.81 and 4.79%, respectively. It generated more accurate results than RFR and SVMR, which is consistent with the previous study [16]. The proposed 3D-ConvNet obtained high

prediction accuracy, with R^2 values and *MNB* values of 0.90 and 2.63%, respectively, which achieved the best performance among all models in this study. Figure 4 displays scatter plots illustrating the measured values of Pb and their corresponding predicted values using the aforementioned models.

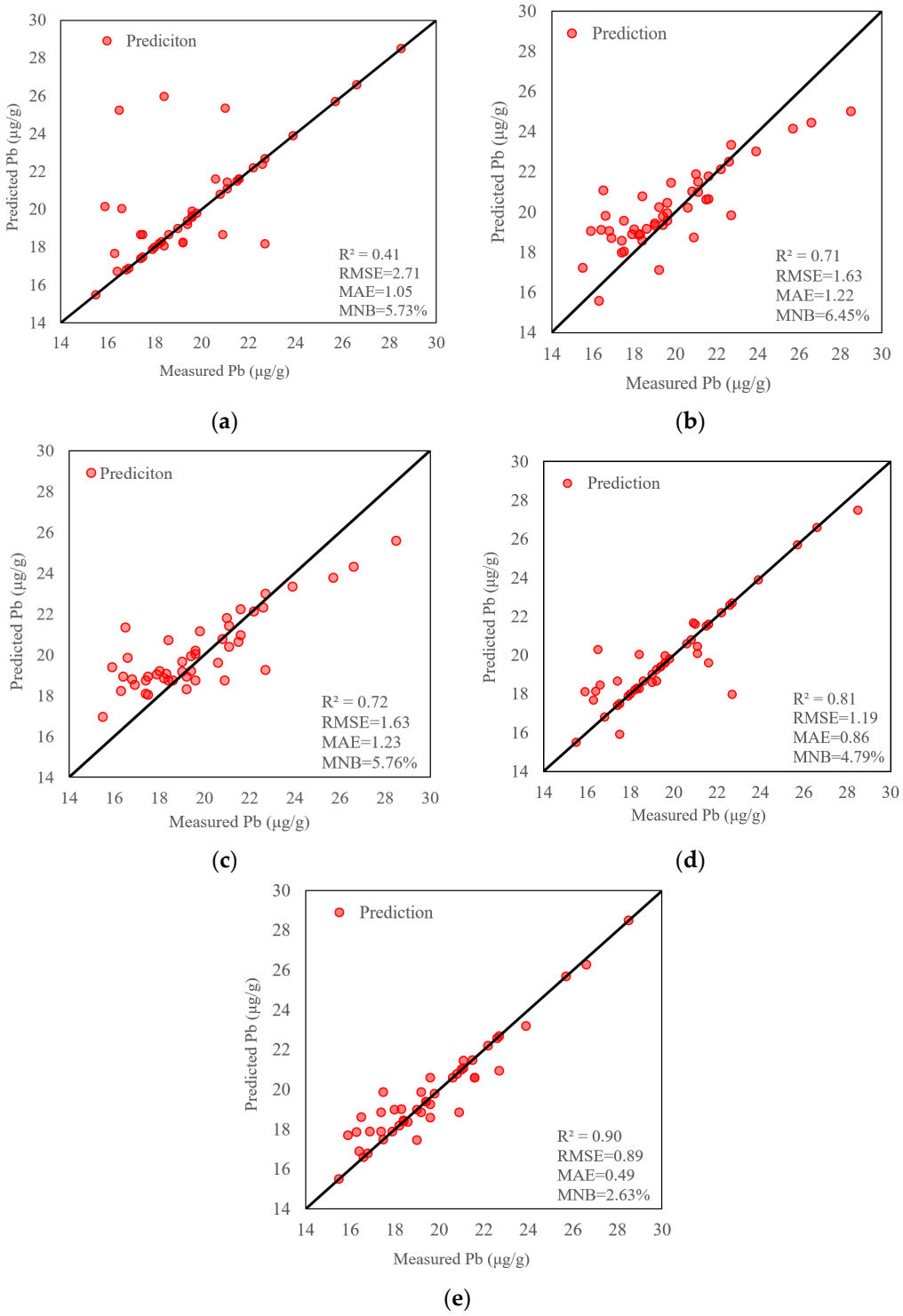


Figure 4. Scatter plots of the measured values of Pb and its predicted values by different models. (**a**) PLSR; (**b**) SVMR; (**c**) RFR; (**d**) GBR; (**e**) 3D-ConvNet.

Overall, it is evident that the proposed 3D-ConvNet effectively captured the intricate spatial–spectral–temporal characteristics of Pb. Consequently, it significantly enhanced

the regression accuracy when compared to conventional machine learning techniques such as PLSR, RFR, SVMR, and GBR models. The findings of this study demonstrate the effectiveness and precision of the developed 3D-ConvNet model in addressing intricate regression problems. In contrast to prior research, this study utilized multi-phase multispectral images to generate spectral data. The results indicate comparable predictive accuracy to that achieved with hyperspectral images, and the method can be used as an alternative to regression using hyperspectral images.

4.3. Pb Distribution Map and Analysis of the Pollution Sources

Given the advantages of 3D-ConvNet compared to other regression models, we utilized the trained 3D-ConvNet model to predict the concentration of Pb using the multiphase remote sensing dataset that we constructed. The resulting spatial distribution of Pb can be observed in Figure 5. In general, the Pb content in urban areas is higher than in most non-urban areas. The Kongzhuang mining area and the Peicheng mining area have higher Pb content compared to other mining areas. Firstly, both mining areas are close to the commercial center of Peixian County, where numerous shops and restaurants exist. The high population density and extensive commercial operations have the potential to elevate the presence of heavy metals in the surrounding environment [50,51]. Secondly, the pollution of heavy metal elements caused by human mining activities is widely recognized [52], and the highly polluted area in Peixian County is very close to the Kongzhuang coal mine and the Peicheng coal mine [53]. Thirdly, the discharge of pollutants from ships could potentially lead to the contamination of nearby soils with heavy metals [54,55]. The nearby Beijing–Hangzhou Grand Canal is a secondary waterway and an important transportation route, with a large number of ships operating daily. Fourthly, the agricultural pollution from surrounding farmland, such as the use of pesticides and fertilizers, may also contribute to the contamination.

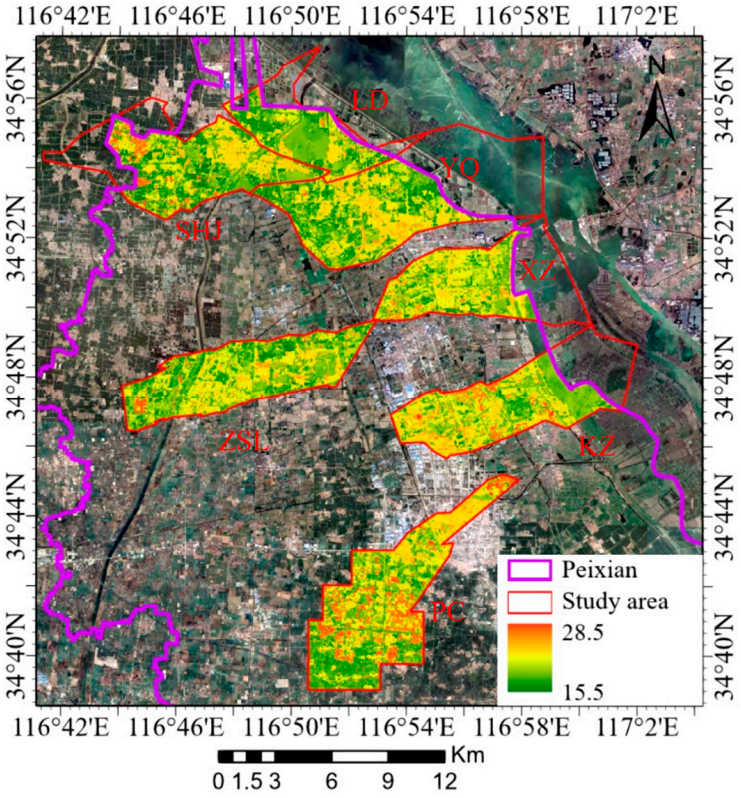


Figure 5. Concentration spatial distribution maps of Pb estimated by 3D-ConvNet.

5. Conclusions

Traditional heavy metal estimation models usually use one temporal period of a hyperspectral image. Hyperspectral images are usually difficult to obtain, but multi-spectral remote sensing images are easier to access. In this study, a 3D-ConvNet model was proposed to estimate the Pb content in soil using the constructed multi-phase multispectral remote sensing images. Experimental results showed the proposed 3D-ConvNet model had obvious superiority and generated more accurate estimation results than traditional models used in this study. The R^2 value of 3D-ConvNet was 0.90, which was improved by 0.09, 0.18, 0.19, and 0.49 compared to PLSR, RFR, SVMR, and GBR, respectively. In addition, the proposed method was much easier to implement due to the easy access to multi-spectral remote sensing images. The spatial distribution map was produced using 3D-ConvNet from the constructed multi-phase multispectral image. After referencing the laboratory test data based on the field sampling, the spatial distribution maps obtained by 3D-CovnNet could accurately indicate the actual Pb distribution. In summary, the proposed 3D-Convnet regression model is an effective approach for heavy metal pollution monitoring based on multi-phase multispectral remote sensing images and could help us make effective heavy metal pollution prevention and control decisions.

However, only multi-spectral images without cloud cover over the study area were used to construct the multi-phase images, which reduced the available images and resulted in unbalanced interval of time phases. Future work will be focused on generating more effective multi-phase remote sensing images to further improve the estimation accuracy, such as multi-source images and longer time-series images.

Author Contributions: Conceptualization, M.T.; data curation, X.Z. and W.L.; funding acquisition, M.T. and M.H.; investigation, M.T. and W.L.; methodology, M.T.; project administration, M.H.; resources, M.H.; validation, M.H.; visualization, X.Z.; writing—original draft, X.Z. and W.L.; writing—review and editing, M.T. All authors have read and agreed to the published version of the manuscript.

Funding: This research was funded by the National Natural Science Foundation of China (Grant No. 52204190 and No. 42271368) and the Fundamental Research Funds for the Central Universities (Grant No. 2021YCPY0113).

Data Availability Statement: Not applicable.

Conflicts of Interest: The authors declare no conflict of interest.

References

1. Qin, G.; Niu, Z.; Yu, J.; Li, Z.; Ma, J.; Xiang, P. Soil heavy metal pollution and food safety in China: Effects, sources and removing technology. *Chemosphere* **2021**, *267*, 129205. [CrossRef] [PubMed]
2. Bier, R.L.; Voss, K.A.; Bernhardt, E.S. Bacterial community responses to a gradient of alkaline mountaintop mine drainage in Central Appalachian streams. *ISME J.* **2015**, *9*, 1378–1390. [CrossRef] [PubMed]
3. Gmochowska, W.; Pietranik, A.; Tyszka, R.; Ettler, V.; Mihaljevic, M.; Dlugosz, M.; Walenczak, K. Sources of pollution and distribution of Pb, Cd and Hg in Wroclaw soils: Insight from chemical and Pb isotope composition. *Geoch* **2019**, *79*, 434–445. [CrossRef]
4. Rai, P.K.; Lee, S.S.; Zhang, M.; Tsang, Y.F.; Kim, K.-H. Heavy metals in food crops: Health risks, fate, mechanisms, and management. *Environ. Int.* **2019**, *125*, 365–385. [CrossRef] [PubMed]
5. Pareja-Carrera, J.; Mateo, R.; Rodriguez-Estival, J. Lead (Pb) in sheep exposed to mining pollution: Implications for animal and human health. *Ecotoxicol. Environ. Saf.* **2014**, *108*, 210–216. [CrossRef]
6. Goodarzi, R.; Mokhtarzade, M.; Zoej, M.J.V. A Robust Fuzzy Neural Network Model for Soil Lead Estimation from Spectral Features. *Remote Sens.* **2015**, *7*, 8416–8435. [CrossRef]
7. Shi, T.; Chen, Y.; Liu, Y.; Wu, G. Visible and near-infrared reflectance spectroscopy—An alternative for monitoring soil contamination by heavy metals. *J. Hazard. Mater.* **2014**, *265*, 166–176. [CrossRef]
8. Cheng, H.; Shen, R.; Chen, Y.; Wan, Q.; Shi, T.; Wang, J.; Wan, Y.; Hong, Y.; Li, X. Estimating heavy metal concentrations in suburban soils with reflectance spectroscopy. *Geoderma* **2019**, *336*, 59–67. [CrossRef]
9. Liu, K.; Zhao, D.; Fang, J.-y.; Zhang, X.; Zhang, Q.-y.; Li, X.-k. Estimation of Heavy-Metal Contamination in Soil Using Remote Sensing Spectroscopy and a Statistical Approach. *J. Indian Soc. Remote Sens.* **2017**, *45*, 805–813. [CrossRef]

10. Rossel, R.A.V.; Walvoort, D.J.J.; McBratney, A.B.; Janik, L.J.; Skjemstad, J.O. Visible, near infrared, mid infrared or combined diffuse reflectance spectroscopy for simultaneous assessment of various soil properties. *Geoderma* **2006**, *131*, 59–75. [CrossRef]
11. Gholizadeh, A.; Boruvka, L.; Saberioon, M.M.; Kozak, J.; Vasat, R.; Nemecek, K. Comparing Different Data Preprocessing Methods for Monitoring Soil Heavy Metals Based on Soil Spectral Features. *Soil Water Res.* **2015**, *10*, 218–227. [CrossRef]
12. Tan, K.; Wang, H.; Zhang, Q.; Jia, X. An improved estimation model for soil heavy metal(loid) concentration retrieval in mining areas using reflectance spectroscopy. *J. Soils Sediments* **2018**, *18*, 2008–2022. [CrossRef]
13. Abdel-Rahman, E.M.; Ahmed, F.B.; Ismail, R. Random forest regression and spectral band selection for estimating sugarcane leaf nitrogen concentration using EO-1 Hyperion hyperspectral data. *Int. J. Remote Sens.* **2013**, *34*, 712–728. [CrossRef]
14. Tan, K.; Wang, H.; Chen, L.; Du, Q.; Du, P.; Pan, C. Estimation of the spatial distribution of heavy metal in agricultural soils using airborne hyperspectral imaging and random forest. *J. Hazard. Mater.* **2020**, *382*, 120987. [CrossRef]
15. Shi, T.; Liu, H.; Chen, Y.; Fei, T.; Wang, J.; Wu, G. Spectroscopic Diagnosis of Arsenic Contamination in Agricultural Soils. *Sensors* **2017**, *17*, 1036. [CrossRef]
16. Wei, L.; Yuan, Z.; Zhong, Y.; Yang, L.; Hu, X.; Zhang, Y. An Improved Gradient Boosting Regression Tree Estimation Model for Soil Heavy Metal (Arsenic) Pollution Monitoring Using Hyperspectral Remote Sensing. *Appl. Sci.* **2019**, *9*, 1943. [CrossRef]
17. Rodriguez-Galiano, V.; Sanchez-Castillo, M.; Chica-Olmo, M.; Chica-Rivas, M. Machine learning predictive models for mineral prospectivity: An evaluation of neural networks, random forest, regression trees and support vector machines. *Ore Geol. Rev.* **2015**, *71*, 804–818. [CrossRef]
18. Chen, Y.; Wu, W. Mapping mineral prospectivity using an extreme learning machine regression. *Ore Geol. Rev.* **2017**, *80*, 200–213. [CrossRef]
19. Tan, K.; Ye, Y.; Cao, Q.; Du, P.; Dong, J. Estimation of Arsenic Contamination in Reclaimed Agricultural Soils Using Reflectance Spectroscopy and ANFIS Model. *IEEE J. Sel. Top. Appl. Earth Observ. Remote Sens.* **2014**, *7*, 2540–2546. [CrossRef]
20. Zheng, J.-Y.; Hao, Y.-Y.; Wang, Y.-C.; Zhou, S.-Q.; Wu, W.-B.; Yuan, Q.; Gao, Y.; Guo, H.-Q.; Cai, X.-X.; Zhao, B. Coastal Wetland Vegetation Classification Using Pixel-Based, Object-Based and Deep Learning Methods Based on RGB-UAV. *Land* **2022**, *11*, 2039. [CrossRef]
21. Fu, Y.; Zhang, T.; Wang, L.; Huang, H. Coded Hyperspectral Image Reconstruction Using Deep External and Internal Learning. *ITPAM* **2022**, *44*, 3404–3420. [CrossRef]
22. Gong, Z.; Zhong, P.; Hu, W. Statistical Loss and Analysis for Deep Learning in Hyperspectral Image Classification. *IEEE Trans. Neural Netw. Learn. Syst.* **2021**, *32*, 322–333. [CrossRef]
23. Hong, S.M.; Baek, S.S.; Yun, D.; Kwon, Y.H.; Duan, H.T.; Pyo, J.; Cho, K.H. Monitoring the vertical distribution of HABs using hyperspectral imagery and deep learning models. *Sci. Total Environ.* **2021**, *794*, 148592. [CrossRef]
24. Liu, J.M.; Xiao, B.; Jiao, J.Z.; Li, Y.S.; Wang, X.Y. Modeling the response of ecological service value to land use change through deep learning simulation in Lanzhou, China. *Sci. Total Environ.* **2021**, *796*, 148981. [CrossRef] [PubMed]
25. Wei, L.; Zhang, Y.; Lu, Q.; Yuan, Z.; Li, H.; Huang, Q. Estimating the spatial distribution of soil total arsenic in the suspected contaminated area using UAV-Borne hyperspectral imagery and deep learning. *Ecol. Indic.* **2021**, *133*, 108384. [CrossRef]
26. Ou, D.; Tan, K.; Lai, J.; Jia, X.; Wang, X.; Chen, Y.; Li, J. Semi-supervised DNN regression on airborne hyperspectral imagery for improved spatial soil properties prediction. *Geoderma* **2021**, *385*, 114875. [CrossRef]
27. Li, Z.; Liu, M.; Chen, Y.; Xu, Y.; Li, W.; Du, Q. Deep Cross-Domain Few-Shot Learning for Hyperspectral Image Classification. *IEEE Trans. Geosci. Remote Sens.* **2022**, *60*, 3057066. [CrossRef]
28. Liu, B.; Yu, A.; Yu, X.; Wang, R.; Gao, K.; Guo, W. Deep Multiview Learning for Hyperspectral Image Classification. *IEEE Trans. Geosci. Remote Sens.* **2021**, *59*, 7758–7772. [CrossRef]
29. Pyo, J.; Duan, H.; Baek, S.; Kim, M.S.; Jeon, T.; Kwon, Y.S.; Lee, H.; Cho, K.H. A convolutional neural network regression for quantifying cyanobacteria using hyperspectral imagery. *Remote Sens. Environ.* **2019**, *233*, 111350. [CrossRef]
30. Niu, C.; Tan, K.; Jia, X.; Wang, X. Deep learning based regression for optically inactive inland water quality parameter estimation using airborne hyperspectral imagery. *Environ. Pollut.* **2021**, *286*, 117534. [CrossRef]
31. Jaihuni, M.; Khan, F.; Lee, D.; Basak, J.K.; Bhujel, A.; Moon, B.E.; Park, J.; Kim, H.T. Determining Spatiotemporal Distribution of Macronutrients in a Cornfield Using Remote Sensing and a Deep Learning Model. *IEEE Access* **2021**, *9*, 30256–30266. [CrossRef]
32. Sun, W.; Zhang, X.; Zou, B.; Wu, T. Exploring the Potential of Spectral Classification in Estimation of Soil Contaminant Elements. *Remote Sens.* **2017**, *9*, 632. [CrossRef]
33. Wang, F.; Gao, J.; Zha, Y. Hyperspectral sensing of heavy metals in soil and vegetation: Feasibility and challenges. *ISPRS J. Photogramm. Remote Sens.* **2018**, *136*, 73–84. [CrossRef]
34. Zhou, X.; Jun, S.; Yan, T.; Bing, L.; Hang, Y.; Quansheng, C. Hyperspectral technique combined with deep learning algorithm for detection of compound heavy metals in lettuce. *Food Chem.* **2020**, *321*, 126503. [CrossRef]
35. Shi, T.; Liu, H.; Chen, Y.; Wang, J.; Wu, G. Estimation of arsenic in agricultural soils using hyperspectral vegetation indices of rice. *J. Hazard. Mater.* **2016**, *308*, 243–252. [CrossRef] [PubMed]
36. Tan, K.; Ma, W.; Chen, L.; Wang, H.; Du, Q.; Du, P.; Yan, B.; Liu, R.; Li, H. Estimating the distribution trend of soil heavy metals in mining area from HyMap airborne hyperspectral imagery based on ensemble learning. *J. Hazard. Mater.* **2021**, *401*, 123288. [CrossRef]
37. Zhang, B.; Guo, B.; Zou, B.; Wei, W.; Lei, Y.; Li, T. Retrieving soil heavy metals concentrations based on GaoFen-5 hyperspectral satellite image at an opencast coal mine, Inner Mongolia, China. *Environ. Pollut.* **2022**, *300*, 118981. [CrossRef]

38. Liu, X.; Wang, Y.; Yan, S. Interferometric SAR time series analysis for ground subsidence of the abandoned mining area in north Peixian using sentinel-1A TOPS data. *J. Indian Soc. Remote Sens.* **2018**, *46*, 451–461. [CrossRef]
39. Lu, Y.; Yang, J.S.; Peng, M.; Li, T.; Wen, D.W.; Huang, X. Monitoring ecosystem services in the Guangdong-Hong Kong-Macao Greater Bay Area based on multi-temporal deep learning. *Sci. Total Environ.* **2022**, *822*, 153662. [CrossRef]
40. Mei, S.; Ji, J.; Geng, Y.; Zhang, Z.; Li, X.; Du, Q. Unsupervised Spatial-Spectral Feature Learning by 3D Convolutional Autoencoder for Hyperspectral Classification. *IEEE Trans. Geosci. Remote Sens.* **2019**, *57*, 6808–6820. [CrossRef]
41. Ioffe, S.; Szegedy, C. Batch normalization: Accelerating deep network training by reducing internal covariate shift. In Proceedings of the 32nd International Conference on International Conference on Machine Learning, Lille, France, 6–11 July 2015; Volume 37, pp. 448–456. [CrossRef]
42. He, K.; Zhang, X.; Ren, S.; Sun, J. Delving Deep into Rectifiers: Surpassing Human-Level Performance on ImageNet Classification. In Proceedings of the IEEE International Conference on Computer Vision 2015, Santiago, Chile, 7–13 December 2015; pp. 1026–1034. [CrossRef]
43. Okujeni, A.; van der Linden, S.; Tits, L.; Somers, B.; Hostert, P. Support vector regression and synthetically mixed training data for quantifying urban land cover. *Remote Sens. Environ.* **2013**, *137*, 184–197. [CrossRef]
44. Moustakidis, S.; Mallinis, G.; Koutsias, N.; Theocharis, J.B.; Petridis, V. SVM-Based Fuzzy Decision Trees for Classification of High Spatial Resolution Remote Sensing Images. *IEEE Trans. Geosci. Remote Sens.* **2012**, *50*, 149–169. [CrossRef]
45. Jebara, T. Multi-task feature and kernel selection for SVMs. In Proceedings of the Twenty-First International Conference on Machine Learning, Banff, AB, Canada, 4–8 July 2004; p. 55. [CrossRef]
46. Summers, D.; Lewis, M.; Ostendorf, B.; Chittleborough, D. Visible near-infrared reflectance spectroscopy as a predictive indicator of soil properties. *Ecol. Indic.* **2011**, *11*, 123–131. [CrossRef]
47. Emadi, M.; Taghizadeh-Mehrjardi, R.; Cherati, A.; Danesh, M.; Mosavi, A.; Scholten, T. Predicting and Mapping of Soil Organic Carbon Using Machine Learning Algorithms in Northern Iran. *Remote Sens.* **2020**, *12*, 2234. [CrossRef]
48. Naghibi, S.A.; Pourghasemi, H.R.; Dixon, B. GIS-based groundwater potential mapping using boosted regression tree, classification and regression tree, and random forest machine learning models in Iran. *Environ. Monit. Assess.* **2016**, *188*, 44. [CrossRef] [PubMed]
49. Friedman, J.; Hastie, T.; Tibshirani, R. Additive logistic regression: A statistical view of boosting. *Ann. Stat.* **2000**, *28*, 337–374. [CrossRef]
50. Cao, S.; Duan, X.; Zhao, X.; Ma, J.; Dong, T.; Huang, N.; Sun, C.; He, B.; Wei, F. Health risks from the exposure of children to As, Se, Pb and other heavy metals near the largest coking plant in China. *Sci. Total Environ.* **2014**, *472*, 1001–1009. [CrossRef]
51. Long, Z.; Huang, Y.; Zhang, W.; Shi, Z.; Yu, D.; Chen, Y.; Liu, C.; Wang, R. Effect of different industrial activities on soil heavy metal pollution, ecological risk, and health risk. *Environ. Monit. Assess.* **2021**, *193*, 20. [CrossRef]
52. Engstrom, D.R.; Fitzgerald, W.F.; Cooke, C.A.; Lamborg, C.H.; Drevnick, P.E.; Swain, E.B.; Balogh, S.J.; Balcom, P.H. Atmospheric Hg Emissions from Preindustrial Gold and Silver Extraction in the Americas: A Reevaluation from Lake-Sediment Archives. *Environ. Sci. Technol.* **2014**, *48*, 6533–6543. [CrossRef]
53. Tang, Q.; Liu, G.; Zhou, C.; Zhang, H.; Sun, R. Distribution of environmentally sensitive elements in residential soils near a coal-fired power plant: Potential risks to ecology and children's health. *Chemosphere* **2013**, *93*, 2473–2479. [CrossRef]
54. Ya-li, C.; Xia, W.; Cheng-qi, Y.; Wen-wen, X.; Wen, S.; Guang-ren, Q.; Zhi-meng, X. Inland Vessels Emission Inventory and the emission characteristics of the Beijing-Hangzhou Grand Canal in Jiangsu province. *Process Saf. Environ. Prot.* **2018**, *113*, 498–506. [CrossRef]
55. Zhuang, W.; Liu, Y.; Chen, Q.; Wang, Q.; Zhou, F. A new index for assessing heavy metal contamination in sediments of the Beijing-Hangzhou Grand Canal (Zaozhuang Segment): A case study. *Ecol. Indic.* **2016**, *69*, 252–260. [CrossRef]

Disclaimer/Publisher's Note: The statements, opinions and data contained in all publications are solely those of the individual author(s) and contributor(s) and not of MDPI and/or the editor(s). MDPI and/or the editor(s) disclaim responsibility for any injury to people or property resulting from any ideas, methods, instructions or products referred to in the content.